Amide bonded polymeric carbon nitride for photocatalytic O_2 activation and NO oxidation

Zixun Fang [a], Min Zhou [b], Zheng Lin [a], Can Yang [a,*], Yidong Hou [a], Jimmy C. Yu [c], Jinshui Zhang [a], Xinchen Wang [a,*]

[a] State Key Laboratory of Photocatalysis on Energy and Environment, College of Chemistry, Fuzhou University, Fuzhou 350002, China
[b] Institute for Energy Research, School of Chemistry and Chemical Engineering, Jiangsu University, Zhenjiang, China
[c] Department of Chemistry, the Chinese University of Hong Kong, Shatin, New Territories, Hong Kong, SAR China

ARTICLE INFO

ABSTRACT

Polymeric carbon nitride (PCN) photocatalysts have the potential to remove NO from ambient air. However, the catalytic performance of PCN is limited by the lack of sufficient active sites to effectively activate molecular oxygen. Herein, we report the construction of photocatalysts consisting of defective-activated-carbon and PCN via amide bond formation. This photocatalyst not only significantly enhances the chemisorption of O_2, but also accelerates the activation of molecular oxygen and oxidation of NO by creating a new electron transport pathway. This work provides a new strategy for polymer photocatalysts to promote molecular oxygen activation by constructing close-contact interfaces through amide bonding.

1. Introduction

Semiconductor photocatalytic technology is a promising and sustainable strategy for converting NO at the ppb level under mild conditions [1–5]. The cost-efficient, visible light-responsive, and metal-lacked polymeric carbon nitride (PCN) with proper electronic structure has been widely used in photocatalytic NO purification [6–10]. The lone pair electrons of nitrogen atoms in PCN could act as Lewis base sites to enhance the NO adsorption and decrease the bond order of N–O, thereby effectively facilitating NO photo-oxidation efficiency [11–14]. It is well-known that insufficient O_2 adsorption sites, competitive adsorption between the O_2 and NO, and sluggish O_2 collision probability restrict the efficiency of conjugated PCN for photocatalytic NO oxidation [15,16]. Molecular oxygen activation (MOA) is a critical step in the formation of oxygen-active species to regulate NO conversion and selectivity [17–19]. Therefore, it is still a challenge to build O_2 adsorption sites, increase O_2 collision, and strengthen O_2 activation, which can speed the deep oxidation of NO based on PCN with inexhaustible solar energy.

Molecular O_2 in the triplet state ($3\Sigma_g^-$) has two unpaired electrons on each of the antibonding π_x^* and π_y^* orbital (Scheme 1) [20,21]. The efficiency of MOA is restricted by the spin-forbidden transitions because of a pair of degenerate π^* antibonding orbitals in O_2 molecules [22]. Introducing excessive electrons to weaken the energy of the O–O bond

is of great significance in boosting MOA [23,24]. The incorporation of carbon atoms in the PCN matrix to construct carbon-rich carbon nitride nanosheets can improve the electronic configuration and surface properties to promote the MOA and improve the performance of photocatalytic desulfurization [25]. A suitable incorporation amount of C_{ring} on the tubular g-C_3N_4 could also remarkably promote the charge carriers separation and enhance the MOA to favor H_2O_2 production [26]. In a word, incorporating carbon-based materials into the PCN skeleton can be considered to strengthen O_2 adsorption and electron enrichment on the surface of the PCN to speed the MOA.

Activated carbon (AC) is prepared by thermolysis and activation processing from carbon-containing raw materials such as lignin, coal, and petroleum coke [27–29]. The well-developed porous structure (<2 nm), a large specific surface area (>1000 m^2/g), and rich surface chemical groups (carboxyl, carbonyl, and hydroxyl) endow AC with strong specific adsorption capacity [30,31]. The aromatic edges formed in the carbonization stage with unsaturated chemical bonds can react with various heterocyclic atoms to form different surface groups, which could achieve adsorption effects by forming strong chemical bonds with adsorbed oxygen molecules [32]. On the one hand, the acidic functional groups on the surface of AC, such as carboxyl groups, could easily form an amide covalent bond with the amino groups of PCN [33]. On the other hand, compared with PCN, AC with a higher work function has a

---

lower Fermi level and exhibits superior electronic storage and conduction capabilities [34].

Herein, we have confined defective AC (DAC) on the surface of PCN to create the amide covalent bond as a close contact interface through an *in-situ* co-pyrolysis strategy to boost MOA and NO photo-oxidation. The effect of oxygen adsorption, electron accumulation, and the interface between the PCN and DAC on MOA and NO photo-oxidation efficiency is estimated. The intelligent gravimetric analyzer (IGA), oxidation-reduction reaction (ORR), electron paramagnetic resonance (EPR), and oxygen temperature-programmed desorption (O_2-TPD) are used to analyze the adsorption and activation process of O_2. As expected, the optimized metal-free DAC/PCN exhibits excellent O_2 activation and NO oxidation efficiency of 49.5% with visible light, which is 2.1 times higher than that of PCN. Combining the in situ diffuse reflectance infrared Fourier-transform spectroscopy (DRIFTS) and EPR test results, we speculate the introduction of DAC could promote the oxidation of NO through the MOA, and generate more superoxide anion radical, elevate the photocatalytic oxidation performance. This work provides an advanced exemplification for designing advanced PCN-based photocatalysts with high MOA ability and air purification capability.

2. Experimental section

2.1. Synthesis of DAC/PCN-x

DAC/PCN-x were prepared by a one-step *in situ* co-pyrolysis method. In a typical process, 2.4 g of dicyandiamide (DCDA) was placed in a mortar and ground for 5 min to form a uniform powder. 20 mg of DAC was then added to the powder and ground for a further 5 min to blend well. The DAC/PCN was obtained by sintering the solid at 550 ℃ for 4 h at a heating rate of 5 ℃/min in nitrogen. For comparison, the obtained samples of DAC/PCN-x were collected by fixing the DCDA and changing the amount of DAC and labeled as DAC/PCN-1 and DAC/PCN-3. The PCN was the same as the above method without adding DAC. The DAC-PCN was obtained by physically mixing PCN and DAC. The synthesis process of DAC/PCN photocatalyst is shown in Figure S1.

2.2. Characterization

The morphology and structure of these catalysts were detected by transmission electron microscopy (TEM, Zeis 912 microscope), X-ray powder diffraction (XRD, Bruker D8 Advance diffractometer with Cu Kα radiation, 2 d sin θ=n λ) [35], scanning electron microscopies (SEM, JEOL mode JSM-6700 F), X-ray photoelectron spectroscopy (XPS, Thermo ESCALAB250 instrument with a monochromatized AlKα line source (200 W), UV−vis spectrophotometer (UV−vis DRS, Varian Cary 500 scan, using BaSO$_4$ as a reference sample), photoluminescence spectra (PL, Edinburgh FI/FSTCSPC 900 spectrophotometer), Raman Spectrometer (LabRAM HR) and BET adsorption isotherm (ASAP 3020). Dynamic adsorption experiments were performed with an intelligent gravimetric analyzer (IGA-003 from Hidden Isochema, UK) [36,37]. The Bruker model A300 spectrometer was used for electron paramagnetic resonance (EPR) measurements. An electrochemical performance test was completed by the electrochemical workstation (CHI 660E). The three-electrode tests were performed in 1 M Na_2SO_4 electrolyte with Ag/AgCl (reference electrode) and platinum electrode (as counter electrode).

2.3. In Situ DRIFTS investigation

In situ DRIFTS measurements were conducted using the VERTEX 70 FTIR spectrometer (Bruker) equipped with an in situ diffuse reflectance cell (Harrick) and a high-temperature reaction chamber (HVC). The reaction chamber contained three gas ports (high-purity He, high-purity O_2, and 100 ppm of NO) and two coolant ports. The total gas flow rate was 100 mL min^{-1}, and the concentration of NO was 5 ppm. The chamber had three windows, including two KBr windows for IR measurements and a quartz window for light irradiation using a KL 2500 LCD lamp (SCHOTT).

The in-situ FT-IR equipment is mainly composed of Tensor II FT-IR spectrometer (Bruker, Germany), in situ reaction cell, gas system, light source, and pre-treatment equipment. Firstly, amount of DAC/PCN and PCN were added into the reactor. To remove the hydrocarbons, H_2O, and CO_2, the He (10 mL min^{-1}) is flowed into the inlet for 30 min at 250 ℃. The sample was then placed and heat-treated in the reaction chamber for 30 min to remove residual carbohydrates, water, and carbon dioxide on the surface of the photocatalysts. The reaction chamber was followed by placing a Tensor II FT-IR spectrometer. The background line was scanned as a baseline. The adsorption gas (10 mL min^{-1} NO) was passed into the reaction vessel. Under dark conditions, the samples were subjected to a 20-minute adsorption reaction. The reaction gas (10 mL min^{-1} NO, 10 mL min^{-1} O_2). Under visible light irradiation, the photocatalytic reaction was carried out for 20 min. The scanned area of the infrared spectra was 4000–500 cm^{-1}.

2.4. Photocatalytic activity measurement

The photocatalytic NO oxidation performance of as-prepared samples was carried out in a continuous flow reactor (1 L) at ambient temperature (25 °C, Figure S2). In detail, 0.1 g of photocatalyst was ultrasonically dispersed into 2 mL of H_2O, and the aqueous suspension was put on the glass dish (diameter of 3 cm), which was further dried at 60 °C to prepare the catalyst film. The dish with the coated sample was heated at for water evaporation to obtain a catalyst film. An LED lamp (Boya Technologies Inc, λ ≥ 420 nm) was used as a light source in low-concentration NO oxidation. The initial concentration of NO (600 ppb) was obtained by diluting the compressed NO with a zero-air generator (Advanced Pollution Instrumentation, Teledyne Technologies Company, Model 701). When the adsorption-desorption equilibrium of the samples was reached, turn on the lamp and start to test the change of NO gas by
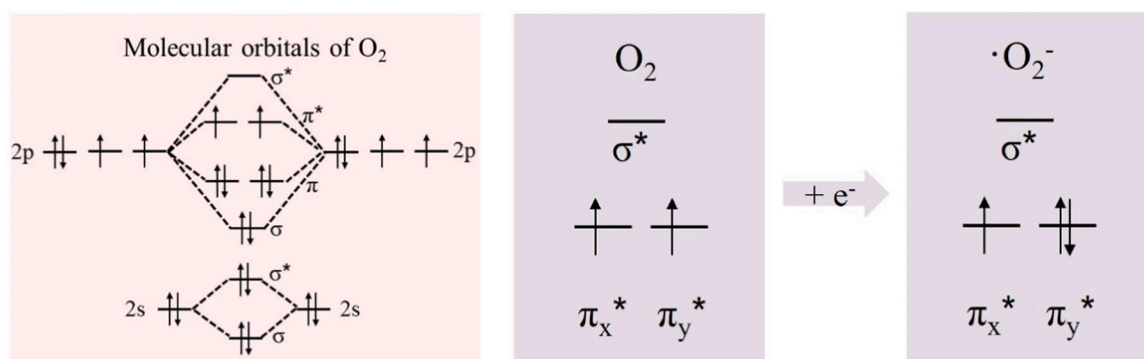
Scheme 1. Molecular orbitals of O_2 and the electron transfer during the formation of superoxide radicals.

using a chemiluminescence NO_x analyzer (Advanced Pollution Instrumentation, Teledyne Technologies Company, Model T200) with a gas flow rate of 1 L min^{-1}. The removal ratio (η) of NO was calculated as η (%) = $(1 - C/C_0) \times 100\%$ [38], where C and C_0 were the concentrations of NO in the outlet and feeding streams, respectively. To check the stability of DAC/PCN, the used catalyst was recovered by centrifugation and then dried in the oven at 60 °C. The dried sample was re-dispersed in 2 mL of deionized water and supplemented with a new catalyst when the catalyst was less than 0.1 g. After drying again, the photocatalytic cycle performance was tested.

3. Results and discussion

Scanning electron microscopy (SEM), transmission electron microscopy (TEM), and atomic force microscopy (AFM) were used to analyze the morphology of the as-synthesized samples. As shown in Fig. 1a, pristine PCN obtained by calcinating DCDA displays a typically thick block nanosheet morphology with a thickness of 100 nm (Figure S3 a and d and S4 a-b). When the DAC is incorporated into the PCN skeleton, the surface gradually becomes rougher and exhibits more fold details compared with PCN, which may provide more active sites for gas adsorption (Fig. 1b and Figure S3 b-c). The layered porous structure of DAC/PCN demonstrates a smaller and thinner thickness of 40 nm (Figure S4 c-d). The C/N ratio obtained by elemental analysis is close to 1, which is higher than that of PCN (0.67), reflecting the successful DAC modification of PCN (Fig. 1c and Figure S5). The X-ray diffraction (XRD) patterns presented in Fig. 1d exhibit the phase structure with no discernible deviations, which is consistent with the Fourier transform infrared (FT-IR) and Raman spectra, indicating maintenance of skeletal structure of PCN structure [39] (Figure S6). The peak of the (002) plane located at 27.4° corresponds to a d-spacing of 0.326 nm, which is ascribed to the interlayer distance of the graphitic-like material. The peak of the (100) plane positioned at 13.0° belongs to the in-plane d-spacing of 0.680 nm. [40–42]. The solid-state ^{13}C NMR spectra were further used to estimate the structure of DAC/PCN (Fig. 1e). Two strong peaks at 156 and 164 ppm in the PCN and DAC/PCN are assigned to C–$(N)_3$ and NH_2–C–$(N)_2$ in the tri-s-triazine units, respectively. A new signal between 100 ppm and 150 ppm of DAC/PCN is observed, which corresponds to the C-C bond in the conjugated aromatic carbons of DAC [43].

The zeta potentials and *in situ* FT-IR were further performed to investigate the content of -NH_2 groups in PCN and DAC/PCN (Fig. 1f-g). It is well-known that -NH_2 groups with the lone pair electrons on nitrogen atoms can act as proton acceptors and acquire positive surface
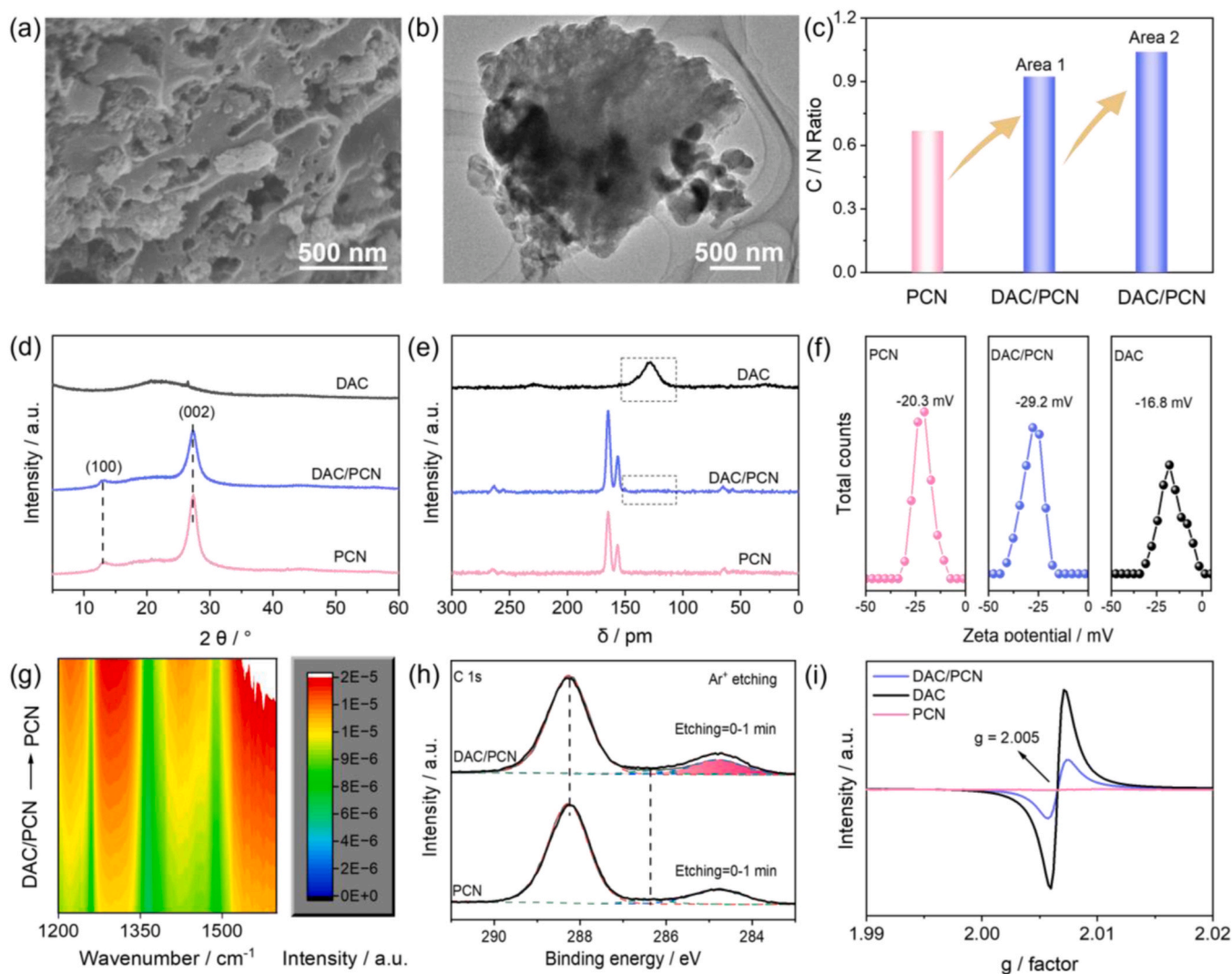

Fig. 1. (a) SEM image and (b) TEM image of DAC/PCN. (c) EDX plot of PCN and DAC/PCN. (d) XRD pattern. (e) Solid state ^{13}C NMR spectra of DAC, PCN, and DAC/PCN. (f) Zeta potential of DAC, PCN, and DAC/PCN. (g) FT-IR spectra recorded after adsorption of trimethyl borate (TB). (h) Ar$^+$ etching of PCN and DAC/PCN. (i) EPR spectra of DAC, PCN, and DAC/PCN.

charge. The zeta potential of DAC/PCN (-29.2 mV) is negative than that of PCN (-20.3 mV), manifesting the reduced amino content in DAC/PCN [44]. The $-NH_2$ groups can also act as Lewis base sites and adsorb acidic trimethyl borate (TB) molecules [45]. In Fig. 1g, the peak intensity at 1490 and 1364 cm^{-1} of DAC/PCN is lower than that of PCN, indicating the significant decrease of $-NH_2$ groups during the *in situ* co-pyrolysis process. X-ray photoelectron spectroscopy (XPS) was employed to study the surface compositions of as-prepared samples. Figure S7a depicts that all samples show C 1s, N 1s, and O 1s signals, where the trace oxygen element probably originates from the adsorbed water and carbon dioxide. The increased C percentage in DAC/PCN-x is attributed to the enhanced amount of DAC. When the DAC/PCN samples are further treated by Ar$^+$ etching (Fig. 1h), the intensity of the C 1s peak is drastically reduced and lower than that of PCN. It is worth noting that the contents of C and N elements show an opposite trend in DAC/PCN-x, indicating the DAC can form a covalent bond with PCN and resulting in the loss of N in $-NH_2$ structure (Figure S7b). Figure S8 show the high-resolution XPS and all the peaks are corrected by the sp^2 C (284.8 eV). In the C 1s spectrum, the sharp and strong peak located at 288.2 eV is ascribed to the triazine ring carbon (N-C$=$N), whereas the peak at 286.3 and 284.8 eV is assigned to the C-NH$_x$ and C-C/C$=$C, respectively [40]. The N 1s spectrum of the as-prepared samples located at 398.7 eV, 400.0 eV, and 401.1 eV, correspond to the C$=$N-C, N-C$_3$, and edge -NH$_x$, respectively. The reduced -NH$_x$ content further indicates that the $-NH_2$ groups of PCN react with the carboxyl groups of DAC to form the amide covalent bond (-CONH-) according to the covalent interaction [33] [44]. The C/N atomic ratio of the obtained samples is determined to be 0.73, 0.76, 0.78, and 0.79 for DAC/PCN-1, DAC/PCN, and DAC/PCN-3, respectively, which is powerful evidence of the successful introduction of DAC (Figure S8c). The solid-state electron paramagnetic resonance (EPR) spectra of the DAC exhibits the strongest signal, demonstrating the surface defects of DAC (Fig. 1i). The surface electronic structure of the PCN is significantly enhanced upon introducing DAC, which is indicated by the intensified spin vibration signals [46] (Figure S9). This also manifests that the tight interaction of DAC and PCN by the amide covalent bond bridging may lead to efficient extension of π−π conjugated delocalization.

UV–vis diffuse reflectance spectroscopy (UV–vis DRS) was performed to estimate the optical properties of samples. A typical semiconductor absorption arising at 450 nm is observed for DAC/PCN, which is similar to the pristine PCN. After post-modification, an enhanced light absorption in the region ranging from 500 to 800 nm is observed, owing to the strong light absorption ability of DAC (Figure S10a). The bandgap of PCN and DAC/PCN is calculated to be 2.78 eV (Figure S10b). Ultraviolet photoelectron spectroscopy (UPS) spectra of PCN and DAC/PCN reveal that the valence band energy (E$_{VB}$) to be 6.41 eV by subtracting the width of the He I UPS spectra from the excitation energy (21.22 eV) (Figure S10c-d). The conduction band energy (E$_{CB}$) is thus estimated at 3.63 eV from the equation of E$_{CB}$= E$_{VB}$ –E$_g$, suggesting the construction of mixture between DAN and PCN [47, 48].

The behaviour of charge carriers was monitored by steady photoluminescence (PL) spectroscopy under an excitation wavelength of 380 nm. In Fig. 2a and Figure S11, the emission peak of DAC/PCN is significantly decreased in comparison with PCN, suggesting that DAC introduction inhibits the recombination of photogenerated electron-hole pairs. Time-resolved photoluminescence spectroscopy (TR-PL) spectra were carried out to investigate the transfer kinetics of charge carriers. The average fluorescence lifetime of DAC/PCN (2.1 ns) is shorter than that of PCN (2.6 ns), implying that the recombination efficiency of photogenerated carriers is reduced after introducing DAC (Fig. 2b). The higher photocurrent and smaller radius of the DAC/PCN sample further indicate strong charge separation efficiency and lower charge transfer resistance than that of PCN (Figure S12). Effective carrier separation can provide sufficient electrons to reduce and activate the adsorbed O$_2$ molecule. In Fig. 2c, the physical and chemical adsorption of O$_2$ on PCN and DAC/PCN were tested by temperature-programmed desorption with O$_2$. The DAC/PCN sample shows a higher and stronger peak located at 123 °C than PCN (115 °C), attributed to the chemisorbed or strong physisorbed desorption of O$_2$, suggesting a high O$_2$ diffusion character and a low O$_2$ activation barrier [14]. The O$_2$ adsorption isotherm of DAC displays type I isotherm, which is attributed to the microporous structure of DAC [37] [49] (Figure S13). The PCN and DAC/PCN deviate from the type I isotherm in the high-pressure range, indicating that the
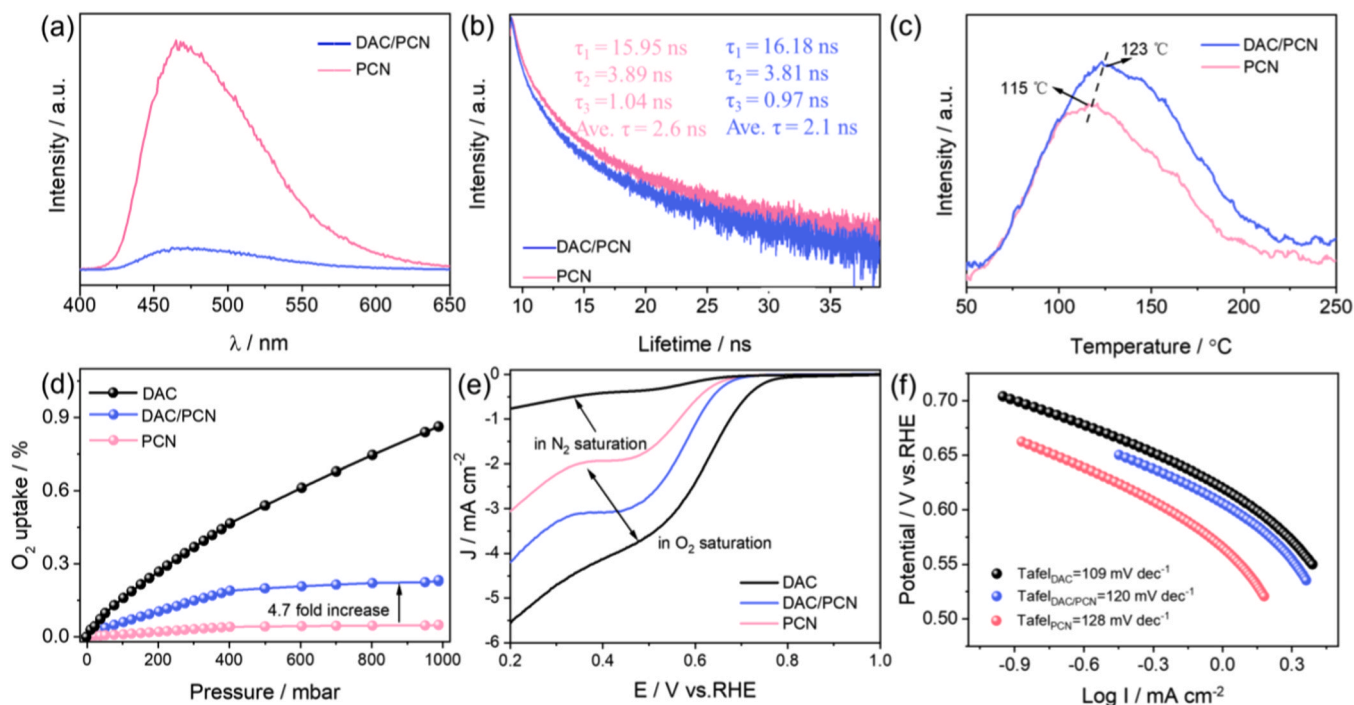

Fig. 2. (a) PL spectra, (b) TR-PL spectra, (c) O$_2$-TPD spectra of PCN and DAC/PCN. (d) IGA tests, (e) ORR tests and (f) Tafel slope of DAC, PCN and DAC/PCN.

mesoporous structure is consistent with BET results (Figure S14). The O_2 uptake capacity of DAC/PCN increases by 4.7 times compared with that of PCN, owing to the introduction of DAC into the PCN matrix (Fig. 2d). In Fig. 2e-f, DAC/PCN exhibits a stronger positive half-wave potential and a lower Tafel slope compared with PCN, which further indicates favorable O_2 reduction ability and faster reaction kinetic for DAC/PCN [50,51]. Moreover, the linear sweep voltammogram (LSV) curves with different rotating speeds and corresponding Koutecky–Levich (K-L) plots of DAC/PCN exhibit prospective O_2 reduction ability compared with PCN and other corresponding comparison samples (Figure S15-17).

To demonstrate the photocatalytic activity of as-synthesized samples, NO photo-oxidation experiments were performed under visible light irradiation. In Fig. 3a, except for the DAC, all the samples reach a maximum of NO removal ratios within 5 min and then tend to be stable. The DAC/PCN possesses the highest NO removal ratio of 49.5%, which is superior to PCN, DAC, and other contrast samples (Figure S18). The PCN and DAC/PCN show relative stability during 20 min, while both of them display a slight decrease in activity when prolonging the irradiation time. The optimal photocatalytic activity of DAC/PCN is ascribed to the tight interface constructed by amide covalent bonds. As demonstrated in Fig. 3b, the fitted first-order rate constant shows that the reaction rate of DAC/PCN (0.118 min^{-1}) is 2.1 times higher than that of PCN (0.056 min^{-1}). The regenerated DAC/PCN sample shows inconspicuous deactivation and exceeds the photocatalytic performance of PCN after four recycling tests, indicating high stability evidenced by the XRD, FTIR, and SEM results (Fig. 3c-d and Figure S19). To elucidate the main type of reactive species generated in the DAC/PCN system, potassium iodide (KI), potassium dichromate ($K_2Cr_2O_7$), tert-butyl alcohol (TBA), and pbenzoquinone (PBQ), and catalase were added into the reaction solution. As shown in Fig. 3e and Figure S20, the PBQ, KI, and $K_2Cr_2O_7$ dramatically decrease the efficiency of NO oxidation, suggesting that the abundant of $^{\bullet}O_2^-$, h^+, e^- are generated in the photocatalytic system of DAC/PCN and PCN. Conversely, the addition of TBA and catalase can only cause little inhibition of NO removal, indicating that $\bullet OH$ and H_2O_2 are not involved in NO photo-oxidation. Electron paramagnetic resonance (EPR) spectra corresponding to $^{\bullet}O_2^-$ are scarcely discernible in the

dark. Under visible-light illumination, DAC/PCN displays a stronger superoxide radical signal than PCN, which is in consistent with the results of quenching experiments (Fig. 3f).

To intuitively reveal the conversion pathways of photocatalytic NO oxidation with PCN and DAC/PCN, an *in situ* DRIFTS was used to reveal the reaction intermediates and products. The background spectrum of *in situ* DRIFTS measurements was recorded before injecting NO into the reaction chamber. In Fig. 4a and Table S1, absorption bands of NO_2^- (860 and 875 cm^{-1}), NO^-/NOH (1051, 1153 and 1174 cm^{-1}), NO_2 (2096 cm^{-1}) can be observed in PCN, which is similar to the DAN/PCN. Other absorption bands of stretching vibration of bidentate nitrite (1111 cm^{-1}), bidentate nitrates (1090–1010 cm^{-1}), monodentate nitrites or chelated nitrites (890 cm^{-1} and 993 cm^{-1}) are the products of NO adsorption. In the case of DAC/PCN, similar adsorption peaks but stronger adsorption intensity of NO adsorption bands can be demonstrated in comparison with PCN (Fig. 4b). A new peak at 900 cm^{-1} assigned to N_2O_4 reveals that the introduction of DAC

can improve the NO adsorption of species for PCN. After adsorption equilibrium is achieved, strengthened N-containing functional groups are detected for PCN and DAC/PCN (Fig. 4c). Notably, enhanced adsorption intensity of the key products located at 866 cm^{-1} (NO_2^-) and 981 cm^{-1} (NO_3^-) are markedly observed in comparison with pure PCN, indicating the increased NO photo-oxidation capacity of DAC/PCN in line with the improvement of ROS production (Fig. 4d). The adsorption process in the dark and the reaction process under light irradiation are displayed in Fig. 4e-f. NO_2, NO^-/NOH, and NO_2^- are the nitro compounds generated by the oxidation of NO by O_2 in the adsorption process, as shown in eqs (1)-(3). After irradiated by the LED light, electrons are excited to the CB of DAC/PCN, which are followed by reacting with adsorbed O_2 to generate $\bullet O_2^-$ radicals eqs (4)-(5). Part of the excited holes remaining in the VB of the DAC/PCN is transferred and reacted with NO to produce NO_3^- eqs (6). These $\bullet O_2^-$ radicals take part in the photocatalytic NO removal process and oxidize NO to NO_3^- eqs (7)-(8).
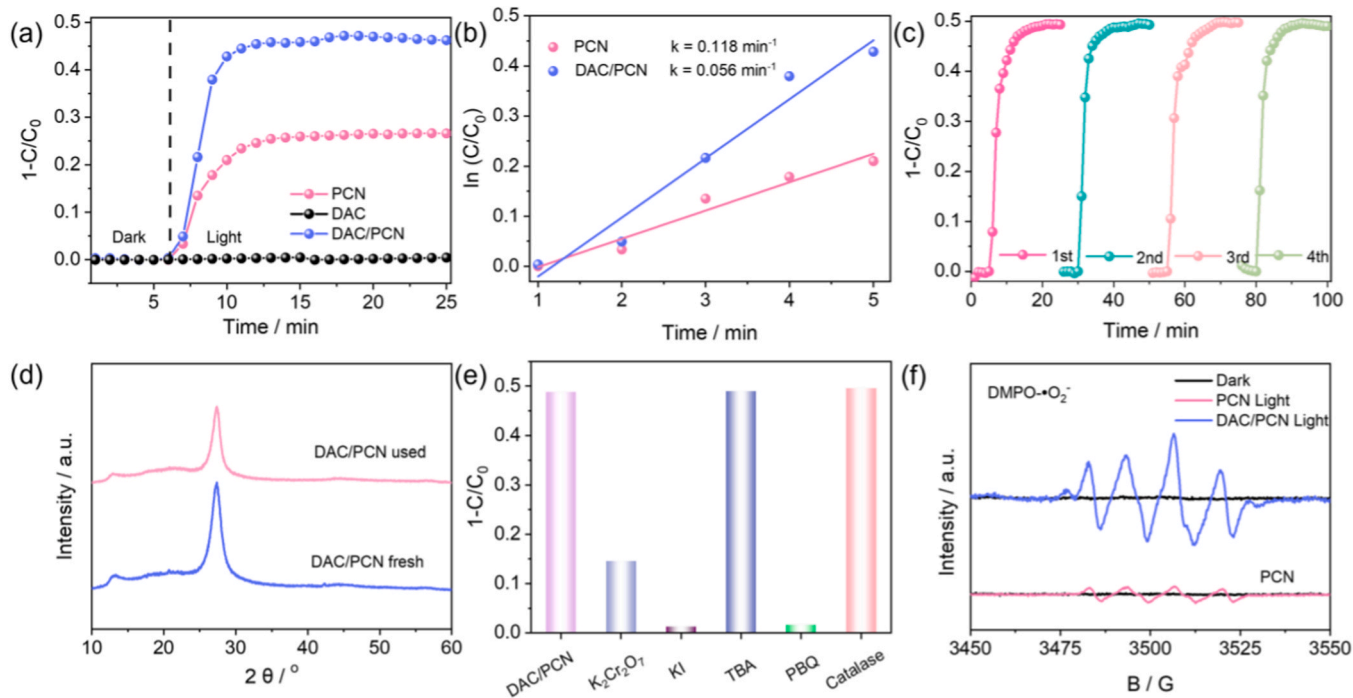

Fig. 3. (a) Visible-light photocatalytic activities of NO photo-oxidation. (b) First-order rate constant of PCN and DAC/PCN. (c) Stability of DAC/PCN sample. (d) XRD spectra of DAC/PCN sample before and after photocatalytic reaction. (e) Photocatalytic activities of DAC/PCN using different capture agents. (f) DMPO spin-trapping EPR spectra of as-prepared samples.
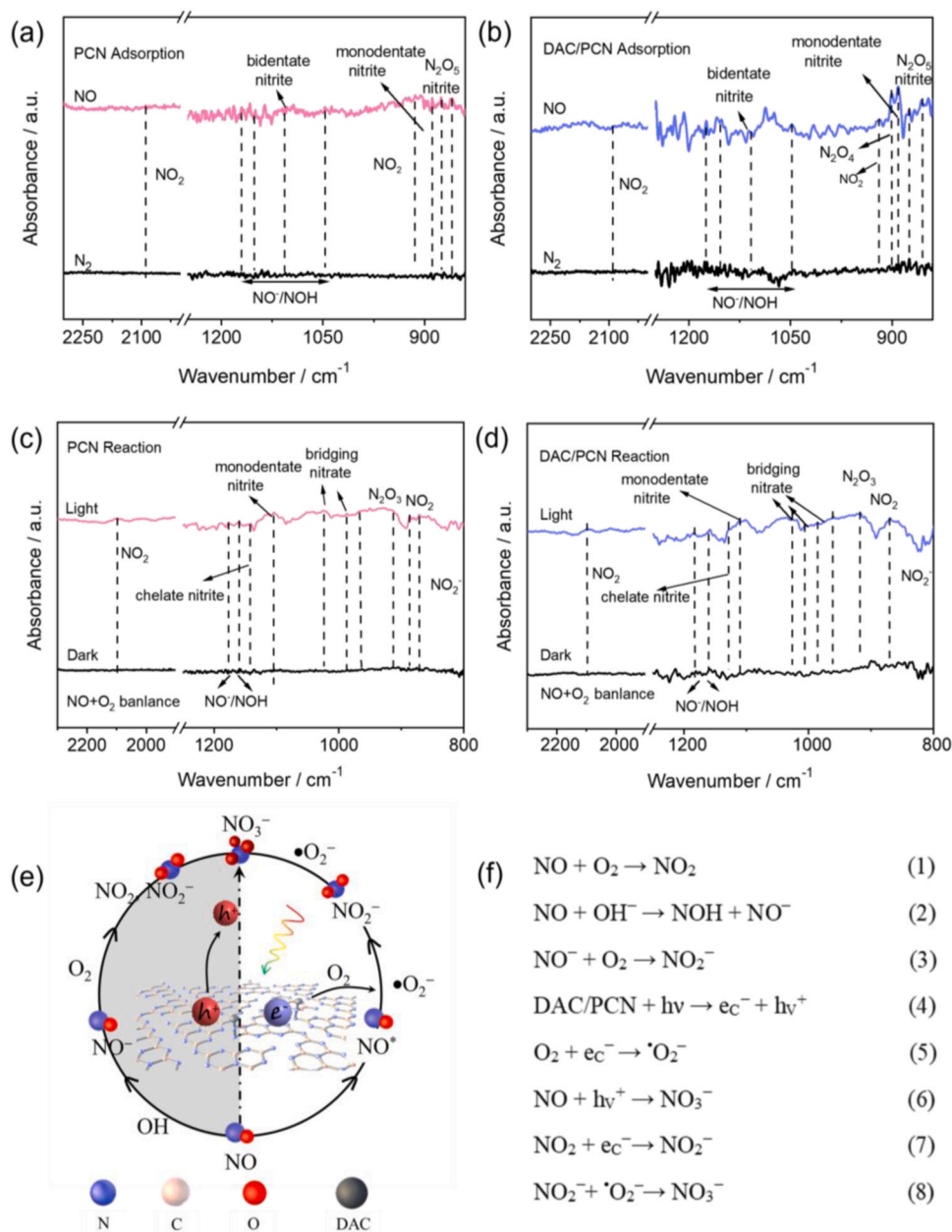
Fig. 4. *In situ* DRIFTS spectra of PCN and DAC/PCN samples (a-b) in the dark and (c-d) under light irradiation. (e-f) Photocatalytic NO oxidation of the DAC/PCN sample (gray represents the adsorption process and white represents the reaction process).

4. Conclusions

In summary, DAC/PCN photocatalysts are synthesized through a simple one-step co-pyrolysis strategy. The O_2 adsorption on the DAC/PCN is enhanced by the introduction of DAC, and the photogenerated electron transfer become more efficient over the close-contact interfaces induced by amide bonding. A mechanism for the enhanced oxygen activation is proposed based on EPR, ORR, and a series of photo-electrochemical measurements. Our findings should be useful for designing next-generation air purification systems.

CRediT authorship contribution statement

Min Zhou: Methodology, Investigation, Formal analysis. **Zheng Lin:** Software, Investigation. **Can Yang:** Writing – original draft, Project administration, Methodology. **Yidong Hou:** Resources, Project administration, Methodology. **Jimmy C. Yu:** Writing – original draft, Conceptualization, Writing – review & editing. **Jinshui Zhang:** Investigation, Supervision. **Xinchen Wang:** Writing – review & editing, Writing – original draft, Visualization, Validation, Conceptualization, Funding acquisition, Project administration, Software, Supervision. **Zixun Fang:** Methodology, Formal analysis, Data curation.

Declaration of Competing Interest

The authors declare that they have no known competing financial interests or personal relationships that could have appeared to influence the work reported in this paper.

Data Availability

Data will be made available on request.

Acknowledgments

Appendix A. Supporting information

Supplementary data associated with this article can be found in the online version at doi:10.1016/j.apcatb.2024.124022.

References

[1] Y. Wang, X. Hu, H. Song, Y. Cai, Z. Li, D. Zu, P. Zhang, D. Chong, N. Gao, Y. Shen, C. Li, Oxygen vacancies in actiniae-like Nb_2O_5/Nb_2C MXene heterojunction boosting visible light photocatalytic NO removal, Appl. Catal. B: Environ. Energy 299 (2021) 120677.

[2] H. Shang, H. Jia, W. Zhang, S. Li, Q. Wang, Q. Yang, C. Zhang, Y. Shi, Y. Wang, P. Li, Y. He, S. Xiao, D. Wang, D. Zhang, Surface hydrogen bond-induced oxygen vacancies of TiO_2 for two-electron molecular oxygen activation and Efficient NO oxidation, Environ. Sci. Technol. 57 (2023) 20400–20409.

[3] Y. Yang, Y. Chen, Z. Li, S. Tang, Y. Li, Z. Fu, S. Yang, M. Yang, H. Xie, Homojunction type of carbon nitride as a robust photo-catalyst for reduction conversion of CO_2 in water vapor under visible light, Chem. Eng. J. 430 (2022) 132668.

[4] Y. Geng, D. Chen, N. Li, Q. Xu, H. Li, J. He, J. Lu, Z-Scheme 2D/2D α-Fe_2O_3/g-C_3N_4 heterojunction for photocatalytic oxidation of nitric oxide, Appl. Catal. B: Environ. Energy 280 (2021) 119409.

[5] Z. Wang, Q. Wei, N. Zhang, X. Shi, M. Chen, Y. Huang, J. Cao, H. Li, W. Ho, S. Lee, Simultaneous polarization engineering and selectivity regulation achieved using polymeric carbon nitride for promoting NOx photo-oxidation, Appl. Catal. B: Environ. Energy 330 (2023) 122582.

[6] F. Guo, B. Hu, C. Yang, J. Zhang, Y. Hou, X. Wang, On-surface polymerization of in-plane highly ordered carbon nitride nanosheets toward photocatalytic mineralization of mercaptan gas, Adv. Mater. 33 (2021) 2101466.

[7] Q. Li, Y. Jiao, Y. Tang, J. Zhou, B. Wu, B. Jiang, H. Fu, Shear stress triggers ultrathin-nanosheet carbon nitride assembly for photocatalytic H_2O_2 production coupled with selective alcohol oxidation, J. Am. Chem. Soc. 145 (2023) 20837–20848.

[8] W. Huang, H. Ming, X. Bian, C. Yang, Y. Hou, K. Ding, J. Zhang, Copper single atoms incorporated in crystalline carbon nitride for efficient photocatalytic activation of peroxymonosulfate toward bisphenol A removal with visible light, Chem. Eng. J. 473 (2023) 145230.

[9] B. Wu, L. Zhang, B. Jiang, Q. Li, C. Tian, Y. Xie, W. Li, H. Fu, Ultrathin porous carbon nitride bundles with an adjustable energy band structure toward simultaneous solar photocatalytic water splitting and selective phenylcarbinol oxidation, Angew. Chem. Int. Ed. 60 (2021) 4815–4822.

[10] M. Kamal Hussien, A. Sabbah, M. Qorbani, M. Hammad Elsayed, P. Raghunath, T. Y. Lin, S. Quadir, H.Y. Wang, H.L. Wu, D.L.M. Tzou, M.C. Lin, P.W. Chung, H. H. Chou, L.C. Chen, K.H. Chen, Metal-free four-in-one modification of g-C_3N_4 for superior photocatalytic CO_2 reduction and H_2 evolution, Chem. Eng. J. 430 (2022) 132853.

[11] M. Zhou, H. Ou, S. Li, X. Qin, Y. Fang, Sc Lee, X. Wang, W. Ho, Photocatalytic air purification using functional polymeric carbon nitrides, Adv. Sci. 8 (2021) 2102376.

[12] C.-Y. Wang, K. Maeda, L.-L. Chang, K.-L. Tung, C. Hu, Synthesis and applications of carbon nitride (CN) family with different carbon to nitrogen ratio, Carbon 188 (2022) 482–491.

[13] G. Liu, Y. Huang, H. Lv, H. Wang, Y. Zeng, M. Yuan, Q. Meng, C. Wang, Confining single-atom Pd on g-C_3N_4 with carbon vacancies towards enhanced photocatalytic NO conversion, Appl. Catal. B: Environ. Energy 284 (2021) 119683.

[14] M. Zhou, L. Zeng, R. Li, C. Yang, X. Qin, W. Ho, X. Wang, Poly(heptazine imide) with enlarged interlayers spacing for efficient photocatalytic NO decomposition, Appl. Catal. B: Environ. Energy 317 (2022) 121719.

[15] P. Zhang, Y. Tong, Y. Liu, J.J.M. Vequizo, H. Sun, C. Yang, A. Yamakata, F. Fan, W. Lin, X. Wang, W. Choi, Heteroatom dopants promote two-electron O_2 reduction for photocatalytic production of H_2O_2 on polymeric carbon nitride, Angew. Chem. Int. Ed. 59 (2020) 16209–16217.

[16] J.H. Geng, L.L. Zhao, M.M. Wang, G.H. Dong, K. Ho, The photocatalytic NO-removal activity of g-C_3N_4 significantly enhanced by the synergistic effect of Pd0 nanoparticles and N vacancies, Environ. Sci. -Nano 9 (2022) 742–750.

[17] H. Li, S. Chen, H. Shang, X. Wang, Z. Yang, Z. Ai, L. Zhang, Surface hydrogen bond network spatially confined BiOCl oxygen vacancy for photocatalysis, Sci. Bull. 65 (2020) 1916–1923.

[18] H. Li, H. Zhu, Y. Shi, H. Shang, L. Zhang, J. Wang, Vacancy-rich and porous NiFe-layered double hydroxide ultrathin nanosheets for efficient photocatalytic NO oxidation and storage, Environ. Sci. Technol. 56 (2022) 1771–1779.

[19] F. Guo, C. Mao, C. Liang, P. Xing, L. Yu, Y. Shi, S. Cao, F. Wang, X. Liu, Z. Ai, L. Zhang, Triangle Cl−Ag_1−Cl sites for superior photocatalytic molecular oxygen activation and NO oxidation of BiOCl, Angew. Chem. Int. Ed. 62 (2023) 51.

[20] S. Cao, Y. Long, S. Xiao, Y. Deng, L. Ma, M. Adeli, L. Qiu, C. Cheng, C. Zhao, Reactive oxygen nanobiocatalysts: activity-mechanism disclosures, catalytic center evolutions, and changing states, Chem. Soc. Rev. 52 (2023) 6838–6881.

[21] Y. Nosaka, A.Y. Nosaka, Generation and detection of reactive oxygen species in photocatalysis, Chem. Rev. 117 (2017) 11302–11336.

[22] Q. Li, F.-t Li, Recent advances in molecular oxygen activation via photocatalysis and its application in oxidation reactions, Chem. Eng. J. 421 (2021) 129915.

[23] J. Xiong, J. Li, H. Huang, M. Zhang, W. Zhu, J. Zhou, H. Li, J. Di, Electronic state tuning over Mo-doped $W_{18}O_{49}$ ultrathin nanowires with enhanced molecular oxygen activation for desulfurization, Sep. Purif. Technol. 294 (2022) 121167.

[24] C. Pan, C. Wang, X. Zhao, P. Xu, F. Mao, J. Yang, Y. Zhu, R. Yu, S. Xiao, Y. Fang, H. Deng, Z. Luo, J. Wu, J. Li, S. Liu, S. Xiao, L. Zhang, Y. Guo, Neighboring sp-hybridized carbon participated molecular oxygen activation on the interface of sub-nanocluster CuO/graphdiyne, J. Am. Chem. Soc. 144 (2022) 4942–4951.

[25] S. Lyu, W. Wu, R. Xiong, C. Yang, B. Sa, J. Zhang, Y. Hou, X. Wang, Carbon-rich carbon nitride nanocatalysts for H_2S selective oxidation, J. Catal. 413 (2022) 992–1004.

[26] H. Luo, T. Shan, J. Zhou, L. Huang, L. Chen, R. Sa, Y. Yamauchi, J. You, Y. Asakura, Z. Yuan, H. Xiao, Controlled synthesis of hollow carbon ring incorporated g-C_3N_4 tubes for boosting photocatalytic H_2O_2 production, Appl. Catal. B: Environ. Energy 337 (2023) 122933.

[27] Y. Jiang, J. Li, Z. Jiang, M. Shi, R. Sheng, Z. Liu, S. Zhang, Y. Cao, T. Wei, Z. Fan, Large-surface-area activated carbon with high density by electrostatic densification for supercapacitor electrodes, Carbon 175 (2021) 281–288.

[28] G. Jiang, R.A. Senthil, Y. Sun, T.R. Kumar, J. Pan, Recent progress on porous carbon and its derivatives from plants as advanced electrode materials for supercapacitors, J. Power Sources 520 (2022) 230886.

[29] D. Zhang, P. Xu, C. Tian, S. Li, T. Xing, Z. Li, X. Wang, P. Dai, Biomass-derived flexible carbon architectures as self-supporting electrodes for energy storage, Molecules 28 (2023) 6377.

[30] H. Jiang, M. Yao, J. Chen, M. Zhang, W. Hong, Advances in biomass-based nanofibers prepared by electrospinning for energy storage devices, Fuel 355 (2024) 129534.

[31] T. Temesgen, E.T. Bekele, B.A. Gonfa, L.T. Tufa, F.K. Sabir, S. Tadesse, Y. Dessie, Advancements in biomass derived porous carbon materials and their surface influence effect on electrode electrochemical performance for sustainable supercapacitors: a review, J. Energy Storage 73 (2023) 109293.

[32] H. Boehm, Some aspects of the surface chemistry of carbon blacks, Carbon 32 (1994) 759–769.

[33] Y. Wang, X. Liu, J. Liu, B. Han, X. Hu, F. Yang, Z. Xu, Y. Li, S. Jia, Z. Li, Y. Zhao, Carbon quantum dot implanted graphite carbon nitride nanotubes: excellent charge separation and enhanced photocatalytic hydrogen evolution, Angew. Chem. Int. Ed. 57 (2018) 5765–5771.

[34] S. Li, Z. Niu, D. Pan, Z. Cui, H. Shang, J. Lian, W. Wu, Efficient photoreduction strategy for uranium immobilization based on graphite carbon nitride/activated carbon nanocomposites, Chin. Chem. Lett. 33 (2022) 3581–3584.

[35] P. Zhang, Y. Tong, Y. Liu, J.J.M. Vequizo, H. Sun, C. Yang, A. Yamakata, F. Fan, W. Lin, X. Wang, W. Choi, Heteroatom dopants promote two-electron O_2 reduction for photocatalytic production of H_2O_2 on polymeric carbon nitride, Angew. Chem. Int. Ed. 59 (2020) 16209–16217.

[36] Y.C. Qin, X.H. Gao, L.F. Shi, L. Zhang, L.H. Duan, L.J. Song, Discrimination of the mass transfer performance of in situ crystallization FCC catalysts by the frequency response method, Acta Phys. -Chim. Sin. 32 (2016) 527–535.

[37] X. Song, G. Qin, C. Cheng, W. Jiang, X. Chen, W. Dai, X. Fu, Oxygen defect-induced $NO^−$ intermediates promoting NO deep oxidation over Ce doped SnO_2 under visible light, Appl. Catal. B: Environ. Energy 284 (2021) 119761.

[38] Y. Cao, R. Zhang, Q. Zheng, W. Cui, Y. Liu, K. Zheng, F. Dong, Y. Zhou, Dual functions of O-atoms in the g-C_3N_4/$BO_{0.2}N_{0.8}$ interface: oriented charge flow in-plane and separation within the interface to collectively promote photocatalytic molecular oxygen activation, ACS Appl. Mater. Interfaces 12 (2020) 34432–34440.

[39] H.B. Ming, D.L. Wei, Y. Yang, B.Q. Chen, C. Yang, J.S. Zhang, Y.D. Hou, Photocatalytic activation of peroxymonosulfate by carbon quantum dots functionalized carbon nitride for efficient degradation of bisphenol A under visible-light irradiation, Chem. Eng. J. 424 (2021) 130296.

[40] V.Wh Lau, B.V. Lotsch, A tour guide through carbon nitride land: structure and dimensionality dependent properties for photo (electro) chemical energy conversion and storage, Adv. Energy Mater. 12 (2021) 2101078.

[41] F. Fina, S.K. Callear, G.M. Carins, J.T.S. Irvine, Structural investigation of graphitic carbon nitride via XRD and neutron diffraction, Chem. Mater. 27 (2015) 2612–2618.

[42] Z. Liang, X. Zhuang, Z. Tang, H. Li, L. Liu, W. Kang, Soft-template induced synthesis of high-crystalline polymeric carbon nitride with boosted photocatalytic performance, J. Mater. Chem. A 9 (2021) 6805–6810.

[43] R.Pd Almeida, R.C. Gomes Aciole, A. Infantes-Molina, E. Rodríguez-Castellón, J. G. Andrade Pacheco, Id.C. Lopes Barros, Residue-based activated carbon from passion fruit seed as support to $H_3PW_{12}O_{40}$ for the esterification of oleic acid, J. Clean. Prod. 282 (2021) 124477.

[44] S. Zhao, T. Guo, X. Li, T. Xu, B. Yang, X. Zhao, Carbon nanotubes covalent combined with graphitic carbon nitride for photocatalytic hydrogen peroxide production under visible light, Appl. Catal. B: Environ. Energy 224 (2018) 725–732.

[45] D. Carriazo, C. Martín, V. Rives, An FT-IR study of the adsorption of isopropanol on calcined layered double hydroxides containing isopolymolybdate, Catal. Today 126 (2007) 153–161.

[46] G. Zhang, W. Huang, Y. Xu, Y. Li, C. He, X. Ren, P. Zhang, H. Mi, Suppressing defects-induced non-radiative recombination for activating the near-infrared photoactivity of red polymeric carbon nitride, Adv. Funct. Mater. 33 (2023) 2305935.

[47] J. Liu, Y. Liu, N.Y. Liu, Y.Z. Han, X. Zhang, H. Huang, Y. Lifshitz, S.T. Lee, J. Zhong, Z.H. Kang, Metal-free efficient photocatalyst for stable visible water splitting via a two-electron pathway, Science 347 (2015) 970–974.

[48] E. Üzer, P. Kumar, R. Kisslinger, P. Kar, U.K. Thakur, S. Zeng, K. Shankar, T. Nilges, Vapor deposition of semiconducting phosphorus allotropes into TiO_2 nanotube arrays for photoelectrocatalytic water splitting, ACS Appl. Nano Mater. 2 (2019) 3358–3367.

[49] S. Lyu, J. Wang, Y. Zhou, C. Wei, X. Liang, Z. Yu, W. Lin, Y. Hou, C. Yang, Structural lithium incorporated with the crystalline poly (triazine imide) frameworks for selective catalytic oxidative desulfurization, Adv. Funct. Mater. (2023) 2310286.

[50] G. Chen, Y. Liu, S. Xue, R. Zhang, H. Lv, J. Zhang, L. Wu, R. Che, Exceptionally bifunctional ORR/OER performance via synergistic atom–cluster interaction, Small (2023) 2308192.

[51] H. Wang, J. Gao, C. Chen, W. Zhao, Z. Zhang, D. Li, Y. Chen, C. Wang, C. Zhu, X. Ke, J. Pei, J. Dong, Q. Chen, H. Jin, M. Chai, Y. Li, PtNi-W/C with atomically dispersed tungsten sites toward boosted ORR in proton exchange membrane fuel cell devices, Nano-Micro Lett. 15 (2023) 143.